Sequentially Responsive Shell-Stacked Nanoparticles for Deep Penetration into Solid Tumors

Jinjin Chen, Jianxun Ding,* Yucai Wang, Jianjun Cheng,* Shengxiang Ji, Xiuli Zhuang, and Xuesi Chen*

Nanomedicine to overcome both systemic and tumor tissue barriers ideally should have a transformable size and surface, maintaining a certain size and negative surface charge for prolonged circulation, while reducing to a smaller size and switching to a positive surface charge for efficient penetration to and retention in the interstitial space throughout the tumor tissue. However, the design of such size and charge dual-transformable nanomedicine is rarely reported. Here, the design of a shell-stacked nanoparticle (SNP) is reported, which can undergo remarkable size reduction from about 145 to 40 nm, and surface charge reversal from −7.4 to 8.2 mV at acidic tumor tissue, for enhanced tumor penetration and uptake by cells in deep tumor tissue. The disulfide-cross-linked core maintains the stability of the particle and prevents undesired premature drug release until the shedding of the shell, which accelerates the cleavage of more exposed disulfide bond sand intracellular drug release. SNP penetrates about 1 mm into xenografted A549 lung carcinoma, which is about four times penetration depth of the nontransformable one. The doxorubicin (DOX)-loaded SNP (SNP/DOX) shows significant antitumor efficacy and nearly eradicates the tumor, substantiating the importance of the design of size and charge dual-transformable nanomedicine.

The main challenge of nanomedicine in cancer therapy is its lack of efficiency of delivering a sufficient payload to and inside the tumor tissue.[1] For example, the first clinically approved liposome nanoformulation, DOXIL, has prolonged blood circulation and enhanced tumor accumulation due to the PEGylation-induced stealth effect and the size-dependent enhanced permeab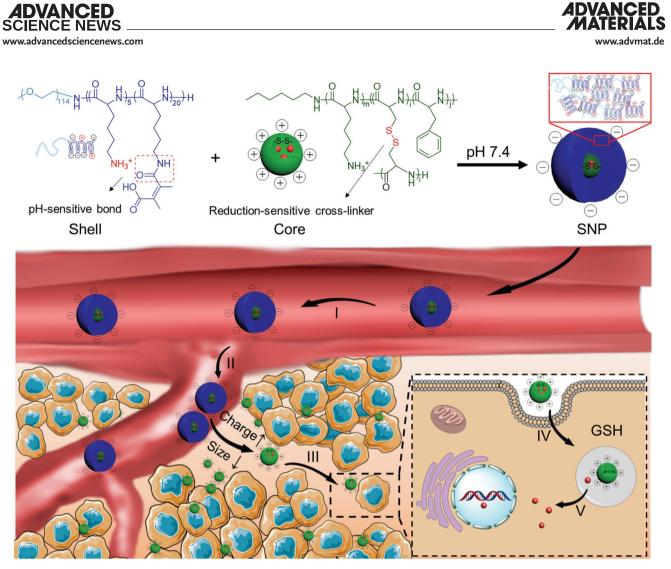ility and retention (EPR) effect.[2] However, once accumulated in a tumor tissue, the negatively charged PEGylated surface and large size become two major barriers for further penetration and internalization.[3]

To address the different requirements of nanomedicine during circulation and penetration, development of smart nanomedicine with size-variable and surface-transformable nanoparticle might provide a good strategy.[4,5] The nanoparticles with variable size and interchangeable charge under tumor stimuli have each been explored. For instance, the nanoplatform, which can reduce their sizes by enzymes or ultraviolet lights, obtains enhanced penetration compared with that of the size-unchangeable one.[5,6] However, the following cell internalization is also burdened with the PEGylated and/or negatively charged surface. On the other hand, nanoparticles with a charge-reversible property under the acidic conditions of tumor tissues can promote cell uptake compared with the non-charge-reversible ones.[7] Unfortunately, the tissue permeability doesn't show significant improvement because of the large size. We hypothesize that smart nanomedicine with both size or charge transformation capability may provide further improved drug delivery efficiency.

Engineering the core–shell polymer nanoparticles with the stimuli-responsive core–shell separation is an ideal and controllable route to construct the dual-convertible nanocarriers. Based on the separable structure, when the nanoparticles accumulate at the tumor site, the PEGylated and negatively charged shells can detach from the nanoparticles for surface transformations. However, after the core–shell separation, the previously reported core–shell structures usually cannot exhibit necessary size reduction mai,nly owing to the thin shell and unstable core. First, for example, the shells formed by the flexible polymers are usually thin and not enough for the subsequently sharp size reduction.[8] Second, after the shedding of PEGylated shells, the nanoparticles usually disassemble and their sizes become larger than before, because the remained cores are unstable and easy to aggregate.[9] The "small to large" transformation is opposite to the requirement of "large to small" change. Therefore, the most promising solution to construct such a dual-convertible nanocarrier is to design a new core–shell structure.

Here, we reported the design of a shell-stacked nanoparticle (SNP) with thick shell and stable core for deep drug delivery

J. Chen, Prof. J. Ding, Prof. S. Ji, Prof. X. Zhuang, Prof. X. Chen
Key Laboratory of Polymer Ecomaterials
Changchun Institute of Applied Chemistry
Chinese Academy of Sciences
Changchun 130022, P. R. China
E-mail: jxding@ciac.ac.cn; xschen@ciac.ac.cn
J. Chen
University of Chinese Academy of Sciences
Beijing 100039, P. R. China
Prof. Y. Wang
School of Life Sciences
University of Science and Technology of China
Hefei 230026, P. R. China
Prof. J. Cheng
Department of Materials Science and Engineering
University of Illinois at Urbana-Champaign
Urbana, IL 61801, USA
E-mail: jianjunc@illinois.edu

ADVANCED
SCIENCE NEWS
www.advancedsciencenews.com

ADVANCED
MATERIALS
www.advmat.de

Scheme 1. Formation and deep tumor penetration of SNP. SNP was composed of the PEGylated and negatively charged shell, and the positively charged and disulfide-cross-linked polypeptide core through electrostatic interaction. Owing to the tumor-microenvironment-mediated multitransformations, SNP could lead to a perfect cascade of drug delivery. I) Long circulation. II) Enhanced accumulation. III) Deep penetration. IV) Promoted internalization. V) Accelerated drug release.

based on a tailor-made core–shell structure. To realize integration of both sharp size reduction and charge reversal for further tissue penetration and cell uptake, the shell was stacked through electrostatic interaction of partially dimethylmaleic anhydride-modified polypeptide (Shell-DMMA) (**Scheme 1**). Based on the original design, the SNP realized remarkable size reduction from around 145 to 40 nm, and surface charge reversal from −7.4 to 8.2 mV after accumulation at the acidic microenvironment of tumor tissue. Moreover, the core was cross-linked by disulfide bonds, which helped maintain the small size after shedding of the shell. Lastly, disintegration of the disulfide-cross-linked core under the intracellular condition accelerated drug release in cells and subsequently induced the upregulated antitumor activity. Owing to the originally designed core–shell structure, the SNP integrated sharp size reduction and necessary charge reversal at the tumor site. The dual-transformable SNP could deliver the antitumor drugs to a much deeper tumor site than the nontransformable one, indicating that the design might be a feasible solution for deep tumor penetration of nanomedicine.

SNP was prepared through a multistep approach, as described in Figure S1 and S2 (Supporting Information). First, the shell of DMMA-modified methoxy poly(ethylene glycol)-*block*-poly(L-lysine) (mPEG$_{113}$-*b*-PLL$_{25}$/DMMA, Shell-DMMA) with charge reversal property was prepared according to our previous work.[10] A disulfide-cross-linked polypeptide copolymer was synthesized through a two-step but one-pot ring-opening polymerization of $N(\varepsilon)$-benzyloxycarbonyl-L-lysine N-carboxyanhydride, and subsequent L-phenylalanine N-carboxyanhydride and L-cystine N-carboxyanhydride using n-hexylamine as an initiator. The obtained copolymer was subsequently deprotected to get the positive-charged and disulfide-cross-linked nanogel of PZLL$_{10}$–P(LP$_7$-*co*-LC$_5$) as the core component.

The ratio of the shell to core was the key factor for controlling the size of SNP. The sizes of SNP under different weight ratios of shell to core were measured and shown in **Figure 1**A. The diameters of the core–shell nanoparticles formed by Shell-DMMA were increased as the weight ratio between shell and core increased. The thickness of the shell can be about three times of the diameter of the core. Finally, the weight ratio of
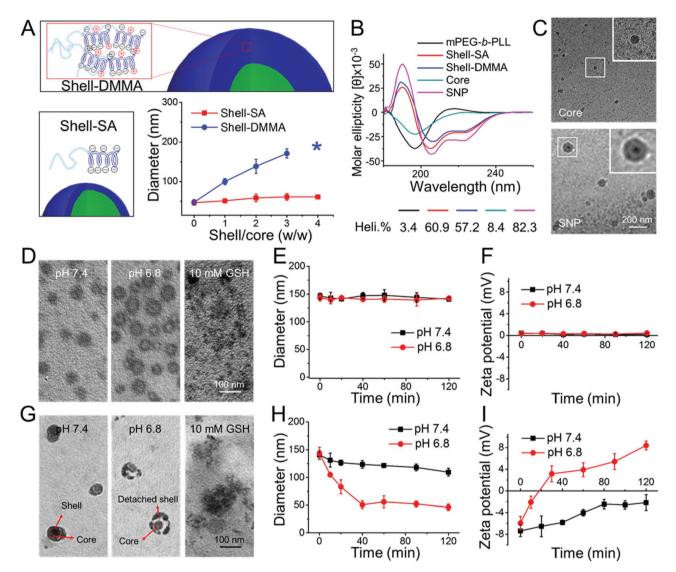
Figure 1. Self-Assembly and sequential stimuli-responsibilities of SNP. A) Size transformation of Shell-DMMA- or Shell-SA-formed nanoparticle under different weight ratios between shell and core. *When the weight ratio of Shell-DMMA and core reached to 4, these nanoparticles tend to adhere to each other. So, the diameter gets much larger and was meaningless. B) Changes in secondary configurations of different components in SNP. C) Morphologies of core and SNP in PBS at pH 7.4 by cryo-TEM. D,G) Morphologies of D) NP and G) SNP in PBS at pH 7.4 or 6.8 without or with 10.0 mM GSH detected by TEM. E,H) Changes of zeta potentials of E) NP and H) SNP in PBS at pH 7.4 or 6.8. F,I) DOX release behaviors of F) NP and I) SNP in PBS at pH 7.4 or 6.8 without or with 10.0 mM GSH.

2:1 was chosen for the formation of SNP. The structure of SNP in solution was then observed by cryogenic transmission electron microscope (cryo-TEM). As shown in Figure 1C, the size of the nanoparticle increased from around 40 to 130 nm after the addition of the shell. A clear core–shell structure could also be observed by cryo-TEM, which further confirmed the successful assembly of the core and shell.

Such a thick shell has never been reported in other core–shell polymer nanoparticles, which might be due to the electrostatic interaction and the rigid α-helical conformation of the polypeptide-based shell. To further prove it, we used the fully negatively charged succinic-anhydride-modified polypeptide-based shell (Shell-SA) as the control to investigate the influence of electrostatic interaction. As shown in Figure 1A, in contrast to the Shell-DMMA-formed nanoparticle, the diameter

of Shell-SA-contained nanoparticle just slightly increased less than 20 nm, and kept unchanged even when the weight ratio of the shell and core increased to 4, because there was no electrostatic interaction among the shell. However, the thick shell was not observed by other works, in which the DMMA-modified polymers were also used as the shell. This might be because the secondary structure of Shell-DMMA might also contribute to the stability of the thick shell. As shown in Figure 1B, after the formation of the core–shell structure, the helicity of SNP increased to 82.3%. Overall, the electrostatic interaction and the rigid α-helical structure might be the two main reasons of the formation of thick and stable shell, enabling the integration of size and surface transformations in one platform.

The key design of SNP was the tumor-microenvironment-mediated transformations of size, charge, and drug release

**ADVANCED
SCIENCE NEWS**
www.advancedsciencenews.com

**ADVANCED
MATERIALS**
www.advmat.de

along with the process of drug delivery into deep tumor cells. To further highlight the advantages of SNP, a nonconvertible nanoparticle (NP) with constant size and surface properties was also prepared and well characterized as a control (Figure S2, Supporting Information). First, the size reduction was important for tumor penetration. As marked in Figure 1G, SNP displayed a clear spherical core–shell structure at pH 7.4, which was detected by TEM. However, when incubated in phosphate-buffered saline (PBS) at pH 6.8, the poly(ethylene glycol) (PEG) corona detached from the core, as pointed in Figure 1G, and subsequently exposed the small-sized core for further penetration. In detail, the size reduction of SNP from about 145 to 40 nm was further proved to be completely achieved within 40 min at pH 6.8 by dynamic light scattering (Figure 1H). By contrast, the size of NP remained in about 140 nm, showing no changes whether at pH 7.4 or 6.8 (Figure 1D,E). The surface charge of SNP kept negative even after 2 h at pH 7.4 (Figure 1I), whereas it turned quickly to be positive just after 20 min at pH 6.8 owing to the detachment of shell. As a comparison, the NP showed neutral both at pH 7.4 and 6.8, as shown in Figure 1F.

Finally, to confirm the intracellularly glutathione (GSH)-accelerated drug release, the morphology changes and drug release behaviors were also determined after incubation with 10.0 mM GSH in Figure 1D,G. The disintegrating structures of both NP and SNP demonstrated the reduction-sensitivities

of the nanocarriers. Doxorubicin (DOX) was chosen as a model drug and loaded into the core with drug loading content of 15.6 wt%. At last, the DOX-loaded SNP (SNP/DOX) was prepared with the final DOX loading content of 5.8 wt% by mixing the shell and the DOX-loaded core at the weight ratio of 1.7:1. As depicted in supplementary Figure S6 (Supporting Information), the cumulative DOX release of both the two formulations were relatively low, i.e., less than 30%, at pH 7.4 without GSH, but reached to a high level of more than 90% after the addition of GSH. All the results indicated the successful tumor-micro-environment-mediated transformations of size, charge, and drug release of SNP, which should be attributed to the smart integration of multifeatures during drug delivery cascade.

Though SNP displayed excellent convertible behaviors responsive to the mimicking tumor microenvironment, the tumor penetration and cell uptake in vitro should be explored for more convincing conclusion. The in vitro evaluation of tumor penetration and cell uptakes of the fluorescein is-thiocyanate (FITC)-marked NP and SNP was carried out to 3D spheroid model (3DSM) derived from A549 human lung cancer cells. The 3DSM was prepared by seeding and incubating cells in a low-attachment 96-well plate as described previously.[11] As shown in **Figure 2**A, NP[FITC] mostly dispersed at the periphery of 3DSM, and only weak fluorescence was detected in the center even until 24 h after co-incubation. By contrast, the FITC
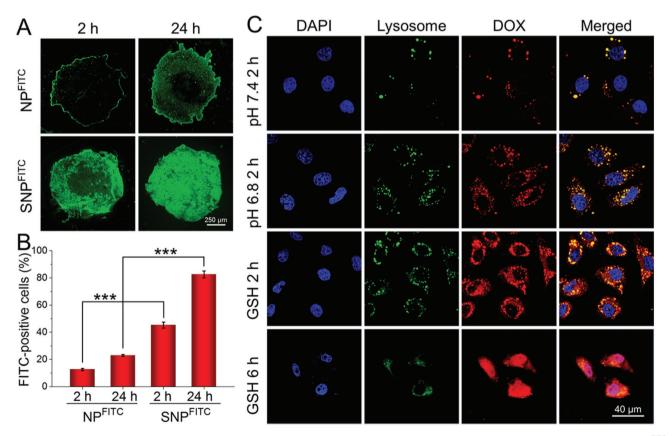

Figure 2. In vitro tumor penetration, cell uptake, and subcellular distribution of SNP toward A549 cells with NP as a control. A) Penetration of NP[FITC] and SNP[FITC] in 3DSMs at pH 6.8 after 2 or 24 h of incubation. B) Quantification of FITC-positive cells of 3DSMs by FCM after incubation with NP[FITC] or SNP[FITC] at pH 6.8 for 2 or 24 h. C) Intracellular DOX distribution in A549 cells after incubation with SNP/DOX under different conditions. The lysosome (green) was marked by LysoTracker Green, and the nuclear (blue) was stained with 4′,6-diamidino-2-phenylindole. The statistical data are presented as mean ± standard deviation (n = 3; ***P < 0.001).

**ADVANCED
SCIENCE NEWS**
www.advancedsciencenews.com

**ADVANCED
MATERIALS**
www.advmat.de

signal of SNP^{FITC} was much deeper and stronger inside 3DSM only after 2 h of treatment compared with that of NP^{FITC}. Furthermore, the cell uptakes of NP^{FITC} and SNP^{FITC} were also evaluated using 3DSM by flow cytometry (FCM) (Figure 2B). Compared to the treatment with NP^{FITC}, the percentages of FITC-positive cells treated with SNP^{FITC} were about 3.5 and 3.7 times higher than those of NP^{FITC} at 2 and 24 h, respectively ($P < 0.001$). However, it seemed there were no significant changes in the cell uptake of NP^{FITC}, because the surface properties of NP^{FITC} kept almost neutral under the slight pH change. These results indicated that the pH-activated tumor tissue and cell permeability to 3DSM were contributed from the transformations of size and charge under tumor tissue condition, suggesting the potential capability of SNP/DOX to deliver antitumor drugs into deep tumor cells.

The subsequent drug release and endosome escape also play important roles in the drug delivery cascades because drugs can be easily degraded by enzymes in lysosome and lose their activities. To reveal the detailed subcellular distribution of DOX after endocytosis, the lysosome was stained with LysoTracker Green and then observed by confocal laser scanning microscopy (CLSM). After co-incubation with SNP/DOX at pH 6.8 for 2 h, the cells exhibited much stronger DOX fluorescence than that at pH 7.4, as shown in Figure 2C. The results demonstrated that the pH-dependent shell shedding facilitated the cell uptake of SNP/DOX. Moreover, in both above groups, the DOX signal almost overlapped with that of the lysosome either at pH 7.4 or 6.8. The results were further demonstrated by FCM in Figure S7 (Supporting Information). To further confirm the GSH-accelerated drug release, the cells were preincubated with 10.0 mM GSH for 2 h. As a consequence, more DOX was released from lysosome to the cytoplasm owing to the upregulated intracellular GSH concentration. The long-term distribution of DOX in the GSH-pretreated A549 cells was also detected after 6 h. Inspiringly, the strong fluorescence intensity was located both in cell cytoplasm and nucleus, which powerfully proved that SNP/DOX could effectively transport DOX to both cell cytoplasm and nucleus by integration of enhanced cell uptake and accelerated intracellular drug release.

The in vivo shell-detachment of SNP was observed by intravital CLSM in **Figure 3**A to further prove the transformation at the tumor site. Just after the injection, the core and shell were almost coincident and colocated in the blood vessels. At 2 h postinjection, the core and shell were accumulated near the blood vessels through the EPR effect, which demonstrated that the coated SNP could not penetrate to deep tumor tissue owing to the large size of about 145 nm. However, after detachment of the shell, the uncoated core travelled much deeper than the coated one because of its small size and weak positive surface. The quantitative analyses of fluorescence intensities also demonstrated the same trend, as depicted in Figure 3B.

To further demonstrate the promoted tumor permeability of SNP after the shedding of shell in tumor tissue, the intravital CLSM observation was also used to track the blood vessel extravasation of NP^{FITC} and SNP^{FITC} in A549 tumors xenografted in nude mice.[11] As shown in Figure 3C and Figure S9 (Supporting Information), after injection of NP^{FITC} for 2 h, the strong green fluorescence signals were almost confined in the edges of blood vessels owing to the EPR effect, which

indicated the nanoparticle with the size of above 100 nm could not penetrate deeply into tumor tissue because of its diffusional hindrance. By contrast, in the SNP^{FITC} group, the weakened green fluorescence was observed in the blood vessels, whereas more green signals were dispersed surrounding the blood vessels, indicating the promoted extravasation of SNP^{FITC}. For detailed analyses of the spatial distribution of the nanoformulations, the fluorescence intensities at the white lines marked in Figure 3C were evaluated, and the intensities were normalized to the strongest dot (Figure 3E). In the NP^{FITC} group, the blood vessels and fluorescence signal almost overlapped. On the contrary, in the SNP^{FITC} group, few fluorescence signals were detected in the blood vessels, whereas much deeper distribution of fluorescence intensity of more than 120.0 μm was observed. The results were also confirmed by the immunofluorescence staining in Figure S10 (Supporting Information). The improved blood vessel extravasation of SNP^{FITC} would certainly benefit the deep penetration in the whole tumor.

To provide insight into the penetration of NP^{FITC} and SNP^{FITC} with dramatically different extravasation in integral tumors, the tumors were harvested after intravital CLSM observation and cut into slices of 10.0 μm. As shown in Figure 3D, a much stronger fluorescence intensity far from the periphery of the tumor occurred in the SNP^{FITC} group compared with that in the NP^{FITC} group. To quantify the ability of penetration, the average fluorescence intensity was analyzed from the periphery to the center of the tumors in three different directions, as depicted in Figure 3F. Inspiringly, the fluorescent intensity remained more than 40% compared to the strongest dot, even in the 1.1 mm depth from the tumor periphery, and also kept at about 15% in the tumor center of SNP^{FITC} group. While in the NP^{FITC} group, the fluorescent intensity decreased remarkably below 10%, even in 0.3 mm from the tumor periphery. The advanced tumor penetration benefited from the reduction of size under slightly acidic microenvironment in tumor tissue, providing the superiority of SNP in cancer treatment.

The in vivo cell uptakes of NP^{FITC} and SNP^{FITC} after tumor penetration were also an important step of drug delivery cascades, which were verified by CLSM in Figure S11 (Supporting Information). The NP^{FITC} almost accumulated in the edge of tumor, and the cells even near the accumulated site showed no obvious fluorescence, as shown in the Enlarged Image 2 (Supporting Information). However, in the SNP^{FITC} group, the fluorescent signals diffused to distant regions. Even in the cells at 100 μm from the tumor periphery, an obvious distribution of fluorescence in tumor cells was observed in the Enlarged Image 2 (Supporting Information) below. The promoted uptake by deep tumor cells in the SNP^{FITC} group further confirmed the probable superiority of SNP in cancer therapy.

The excellent tumor penetration of SNP/DOX urged us to give further insights into its in vivo antitumor efficacy. First of all, the extended blood circulation and enhanced tumor accumulation of SNP/DOX were proved in **Figure 4**A,B, respectively. Both NP/DOX and SNP/DOX showed prolonged blood circulation with the elimination half-life ($t_{1/2}$) of 20.9 and 19.7 h, respectively. While free DOX showed rapid clearance during circulation ($t_{1/2} = 11.4$ h). Moreover, NP/DOX and SNP/DOX also exhibited significantly increased area under the curve in blood, i.e., 9.7 and 7.0 times higher than that in the free

**ADVANCED
SCIENCE NEWS**

www.advancedsciencenews.com
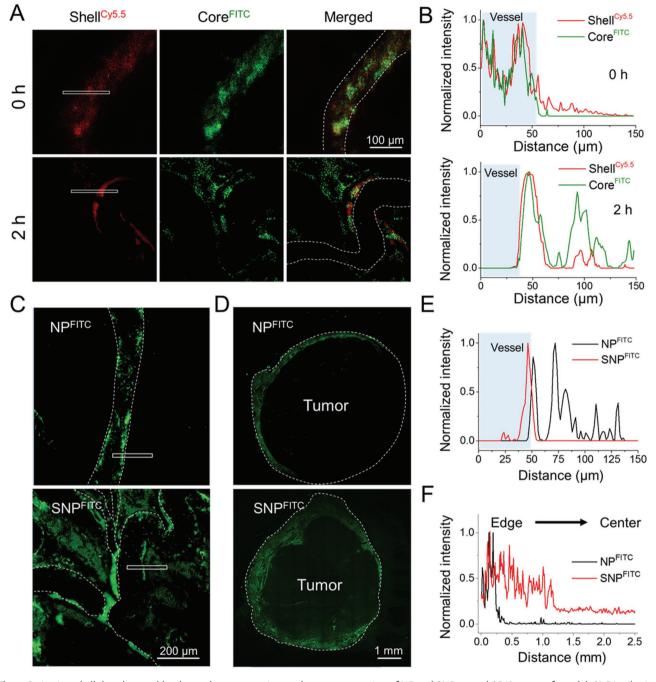
**ADVANCED
MATERIALS**

www.advmat.de

Figure 3. In vitro shell-detachment, blood vascular extravasation, and tumor penetration of NP and SNP toward A549 xenograft model. A) Distribution of Shell$^{Cy5.5}$ and Core^{FITC} by intravital CLSM microimages in A549 lung carcinoma-xenografted mouse model at 0 or 2 h postinjection. The white dotted line indicated the locations of blood vessels. B) Time-dependent distribution of Shell$^{Cy5.5}$ and Core^{FITC} at 0 h (top) and 2 h (bottom) after injection. C) Blood vascular extravasation of NP^{FITC} and SNP^{FITC} by intravital CLSM microimages in A549 lung carcinoma-xenografted mouse model at 2 h postinjection. D) Penetration overviews of NP^{FITC} and SNP^{FITC} in the whole tumor. E) Depth-dependent distribution of NP^{FITC} and SNP^{FITC} after extravasation. F) Tumor penetration quantification of NP^{FITC} and SNP^{FITC}.

DOX group, owing to the stealth effect induced by PEGylation. In Figure 4B,C, the increased intensity of DOX in the tumor of SNP/DOX group was about 1.8 and 1.4 times of those in the free DOX and NP/DOX groups, respectively, which resulted from both the EPR effect-mediated accumulation and size-mediated penetration.

Last but not least, the nanoformulations minimized the toxicity of DOX, which was proved by the evaluation of maximum tolerated dose, as shown in Figure S12 (Supporting Information). The mice treated with NP/DOX or SNP/DOX at DOX dosage even of 20.0 mg per kg body weight (mg (kg BW)$^{-1}$) showed no significant weight loss. However, the body
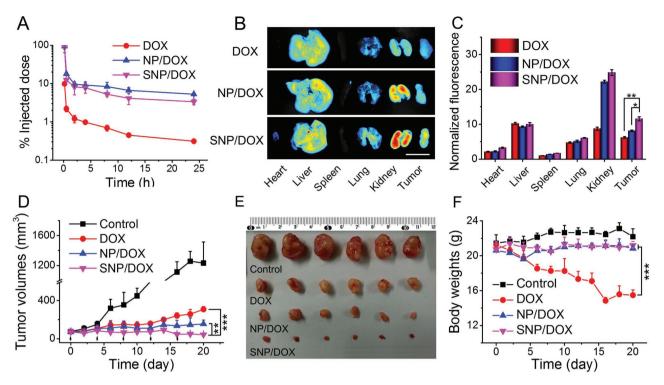
Figure 4. In vivo pharmacokinetics, biodistributions, and antitumor efficiencies of NP/DOX and SNP/DOX toward A549 lung-cancer-xenografted mouse model. A) Pharmacokinetics of DOX, NP/DOX, and SNP/DOX after intravenous injection into Sprague–Dawley rats at a DOX dose of 5.0 mg (kg BW)$^{-1}$. B) Biodistribution of DOX in A549 tumor-bearing BALB/c nude mice after intravenous injection of free DOX, NP/DOX, and SNP/DOX at a DOX dose of 5.0 mg (kg BW)$^{-1}$ for 12 h. Scale bar = 0.5 cm. C) Quantification of DOX intensities in different organs and tumors. D) Inhibition of A549 lung carcinoma in nude mice after treatment with PBS, free DOX, NP/DOX, or SNP/DOX at a DOX dose of 5.0 mg (kg BW)$^{-1}$ on day 0, 4, 8, 12, and 16. E) Images of tumors stripped from the treated mice at the end of the experiment. F) Body weight changes of different groups in experiment of tumor inhibition. All statistical data are presented as mean ± standard deviation. ($n = 3$ for (A,C); $n = 6$ for (D,F); *$P < 0.05$, **$P < 0.01$, ***$P < 0.001$).

weights of the mice treated with free DOX at the dosage of 10.0 or 20.0 mg (kg BW)$^{-1}$ decreased dramatically and even died completely. Further evaluation of biochemical parameters, e.g., creatine kinase, alanine aminotransferase, aspartate transaminase, and blood urea nitrogen, also showed no significant differences between nanoformulation-treated and healthy mice (Figure S13, Supporting Information).

The in vivo therapeutic efficacy of SNP/DOX was compared with those of free DOX and NP/DOX on the subcutaneous A549 tumor-bearing nude mouse model. As shown in Figure 4D, free DOX exhibited the modest antitumor efficacy with tumor inhibition rate of 75% compared with the control group treated with PBS, whereas NP/DOX showed 87% tumor inhibition rate. The enhanced efficacy should be attributed to the increased circulation and accumulation after being loaded into NP. Moreover, the tumor in the SNP/DOX group was largely eradicated with the inhibition of 97%. The tumors collected and photographed in Figure 4E at the end of treatment also intuitionally demonstrated the same trend. The superior antitumor efficacy was predictable based on the excellent tumor penetration and cell uptake of SNP. Moreover, both NP/DOX and SNP/DOX showed reduced systemic toxicity as revealed by the stable body weight compared with that in the free DOX group, as depicted in Figure 4F. In Figure S14A (Supporting Information), hematoxylin and eosin staining also showed that the tumor treated with PBS as a control consisted of tightly

packed tumor cells, whereas those in the free DOX, NP/DOX, and SNP/DOX groups exhibited typically apoptotic symbols of pyknosis, karyorrhexis, and karyolysis. Further immunofluorescence staining of apoptosis- and proliferation-related proteins also showed the similar results. In Figure S14 (Supporting Information), most tumor cells treated with SNP/DOX were caspase-3-positive and survivin-negative. These histopathology and immunofluorescence analyses strongly confirmed the improved antitumor efficacy of SNP/DOX.

In summary, a SNP subject to both substantial particle size reduction and surface charge reversal in tumor microenvironment was designed and prepared for the first time based on the electrostatic interaction and the rigid α-helical conformation of polypeptides. SNP exhibited the remarkable features in favor of controlled systemic antitumor drug delivery, maintaining certain size of about 145 nm and negative surface charge of −7.4 mV for prolonged circulation, while reducing to a smaller size of around 40 nm and transforming to a positive surface charge of 8.2 mV for efficient penetration to and retention in the interstitial space throughout the tumor tissue. The dual-transformable nanomedicine could penetrate about four times deeper than that of the nontransformable one in A549 lung carcinoma. More importantly, such size and surface charge dual-transformable nanomedicine almost eradicated the xenografted A549 lung carcinoma in mice. The original design of stacked shell ensured the integration of size reduction and charge

reversal in one platform. Inspired by the enhanced tumor penetration and antitumor efficiency of SNP, such design of dual-transformation provided a feasible solution for deep delivery of nanomedicine.

Supporting Information

Supporting Information is available from the Wiley Online Library or from the author.

Conflict of Interest

The authors declare no conflict of interest.

Keywords

cancer therapy, charge reversal, nanomedicine, sequential responsiveness, size reduction

[1] a) M. R. Dreher, W. Liu, C. R. Michelich, M. W. Dewhirst, F. Yuan, A. Chilkoti, *J. Natl. Cancer Inst.* **2006**, *98*, 335; b) H. Cabral, Y. Matsumoto, K. Mizuno, Q. Chen, M. Murakami, M. Kimura, Y. Terada, M. R. Kano, K. Miyazono, M. Uesaka, N. Nishiyama, K. Kataoka, *Nat. Nanotechnol.* **2011**, *6*, 815.

[2] a) Y. C. Barenholz, *J. Controlled Release* **2012**, *160*, 117; b) T. Safra, F. Muggia, S. Jeffers, D. Tsao-Wei, S. Groshen, O. Lyass, R. Henderson, G. Berry, A. Gabizon, *Ann. Oncol.* **2000**, *11*, 1029.

[3] a) R. K. Jain, T. Stylianopoulos, *Nat. Rev. Clin. Oncol.* **2010**, *7*, 653; b) S. D. Li, L. Huang, *J. Controlled Release* **2010**, *145*, 178; c) H. Hatakeyama, H. Akita, H. Harashima, *Adv. Drug Delivery Rev.* **2011**, *63*, 152; d) J. Z. Du, T. M. Sun, W. J. Song, J. Wu, J. Wang, *Angew. Chem., Int. Ed.* **2010**, *49*, 3621; e) L. Tang, X. Yang, Q. Yin, K. Cai, H. Wang, I. Chaudhury, C. Yao, Q. Zhou, M. Kwon, J. A. Hartman, *Proc. Natl. Acad. Sci. USA* **2014**, *111*, 15344.

[4] a) Q. Sun, X. Sun, X. Ma, Z. Zhou, E. Jin, B. Zhang, Y. Shen, E. A. Van Kirk, W. J. Murdoch, J. R. Lott, *Adv. Mater.* **2014**, *26*, 7615; b) J. Z. Du, X. J. Du, C. Q. Mao, J. Wang, *J. Am. Chem. Soc.* **2011**, *133*, 17560.

[5] C. Wong, T. Stylianopoulos, J. Cui, J. Martin, V. P. Chauhan, W. Jiang, Z. Popovi, R. K. Jain, M. G. Bawendi, D. Fukumura, *Proc. Natl. Acad. Sci. USA* **2011**, *108*, 2426.

[6] R. Tong, H. H. Chiang, D. S. Kohane, *Proc. Natl. Acad. Sci. USA* **2013**, *110*, 19048.

[7] Y. Lee, T. Ishii, H. J. Kim, N. Nishiyama, Y. Hayakawa, K. Itaka, K. Kataoka, *Angew. Chem., Int. Ed.* **2010**, *49*, 2552.

[8] a) X. Z. Yang, X. J. Du, Y. Liu, Y. H. Zhu, Y. Z. Liu, Y. P. Li, J. Wang, *Adv. Mater.* **2014**, *26*, 931; b) J. Li, X. Yu, Y. Wang, Y. Yuan, H. Xiao, D. Cheng, X. Shuai, *Adv. Mater.* **2014**, *26*, 8217; c) J. Chen, J. Ding, C. Xiao, X. Zhuang, X. Chen, *Biomater. Sci.* **2015**, *3*, 988.

[9] a) W. Gao, R. Langer, O. C. Farokhzad, *Angew. Chem., Int. Ed.* **2010**, *49*, 6567; b) T. Suma, K. Miyata, Y. Anraku, S. Watanabe, R. J. Christie, H. Takemoto, M. Shioyama, N. Gouda, T. Ishii, N. Nishiyama, K. Kataoka, *ACS Nano* **2012**, *6*, 6693.

[10] J. Chen, J. Ding, Y. Zhang, C. Xiao, X. Zhuang, X. Chen, *Polym. Chem.* **2015**, *6*, 397.

[11] H. J. Li, J. Z. Du, X. J. Du, C. F. Xu, C. Y. Sun, H. X. Wang, Z. T. Cao, X. Z. Yang, Y. H. Zhu, S. Nie, J. Wang, *Proc. Natl. Acad. Sci. USA* **2016**, *113*, 4164.